How to cite: *Angew. Chem. Int. Ed.* **2023,** *62,* e202215071
International Edition: doi.org/10.1002/anie.202215071
German Edition: doi.org/10.1002/ange.202215071

Luminescence

Diboraanthracene-Doped Polymer Systems for Colour-Tuneable Room-Temperature Organic Afterglow

Justina Jovaišaitė, Sven Kirschner, Steponas Raišys, Gediminas Kreiza, Paulius Baronas, Saulius Juršėnas, and Matthias Wagner**

Abstract: Organic ultralong room temperature phosphorescence (RTP), or organic afterglow, is a unique phenomenon, gaining widespread attention due to its far-reaching application potential and fundamental interest. Here, two laterally expanded 9,10-dimesityl-dihydro-9,10-diboraanthracene (DBA) derivatives are demonstrated as excellent afterglow materials for red and blue-green light emission, which is traced back to persistent thermally activated delayed fluorescence and RTP. The lateral substitution of polycyclic DBA scaffold, together with weak transversal electron-donating mesityl groups, ensures the optimal molecular properties for (reverse) intersystem crossing and long-lived triplet states in a rigid poly(methyl methacrylate) matrix. The achieved afterglow emission quantum yields of up to 3 % and 15 %, afterglow lifetimes up to 0.8 s and 3.2 s and afterglow durations up to 5 s and 25 s (for red and blue-green emitters, respectively) are attributed to the properties of single molecules.

Introduction

Organic ultralong room temperature phosphorescence (RTP), often referred to as organic afterglow, is an exceptional phenomenon which exhibits a long emission lifetime, exceeding 100 ms.[1] Recently, it has attracted extensive scientific interest due to its promising widespread applications in multidisciplinary fields, such as data encryption,[2,3] anti-counterfeiting,[4] bioimaging,[5,6] and sensing.[6] Most of the aforementioned application fields require phosphorescence to be long-lasting and efficient, which are in principle conflicting design goals. This is because the increase of phosphorescence radiative rate enhances its quantum efficiency, thereby reducing its lifetime.[7] Thus, not only practical but also fundamental interest motivates the research efforts in this field. The strategies employed in order to achieve long (>100 ms) and efficient (>5 %) pure organic afterglow systems rely on the fulfilment of two main conditions: (i) promotion of the intersystem crossing (ISC) from S_1 to T_n for the efficient triplet generation; and (ii) suppression of the radiative and non-radiative decay of triplet state ($T_1 \rightarrow S_0$) to prolong its lifetime.[8] The first condition requires the small energy gap and sufficient spin-orbit coupling between S_1 and T_n states of different character,[9–11] while the second one implicates the locally excited (LE) character of T_1 and highly rigid environment, protected from oxygen and moisture.[8]

Thus far, many reported room temperature (RT) afterglow systems have been based on aggregation-induced emission,[12] including crystal engineering,[13,14] H-aggregation,[15] π-π stacking,[16] host-guest interaction[17] or even supramolecular assembly,[18] all of which facilitate the stabilization of triplet states and reduce the non-radiative quenching. However, the practical implementation of aggregated molecular states, especially crystals, may be hindered due to their brittleness and limited processability. Furthermore, the crystallization of the molecules greatly enhances triplet exciton migration, which may lead to capture at impurity or defect-related traps, causing the quenching of excited states. Thus, the focus has shifted towards polymer-based amorphous organic systems due to their appeal with regard to practical applications.[19,20] The most attractive approach in terms of fabrication is a simple physical blending of polymer and guest molecules, such that the appearance of noncovalent bonds would ensure a rigid environment for both reduced excitonic and vibrational quenching of triplet excitons, without affecting the excited states of molecules.[19,21] In this case, the chromophore itself must demonstrate the combination of long and efficient RTP; therefore, the same contradiction of long and efficient phosphorescence needs to be addressed.

In this work, we present two 9,10-dimesityl-9,10-diboraanthracene (DBA) compounds as a new class of organic RT emission afterglow materials. The mesityl groups not only render the materials air-and moisture-stable,[22,23] but

[*] J. Jovaišaitė, S. Raišys, G. Kreiza, P. Baronas, S. Juršėnas
Institute of Photonics and Nanotechnology, Vilnius University
Saulėtekis av. 3, 10257 Vilnius (Lithuania)
E-mail: justina.jovaisaite@ff.vu.lt

S. Kirschner, M. Wagner
Institut für Anorganische Chemie, Goethe-Universität Frankfurt
Max-von-Laue-Strasse 7, 60438 Frankfurt a. Main (Germany)
E-mail: matthias.wagner@chemie.uni-frankfurt.de

S. Kirschner
EaStCHEM School of Chemistry, The University of Edinburgh
David Brewster Road, Edinburgh EH9 3FJ (UK)

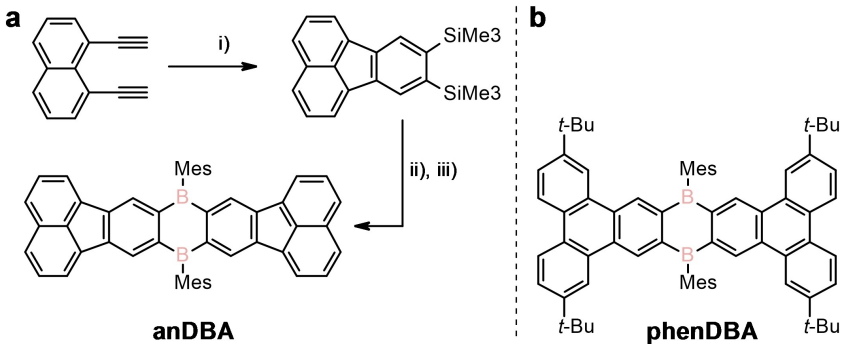

Scheme 1. Synthesis and Lewis structure of anDBA (a) and Lewis structure of phenDBA (b). Reagents and conditions: i) $Me_3SiC{\equiv}CSiMe_3$ (excess), $CpCo(CO)_2$ (10 mol%), reflux temperature, 10 h; ii) BBr_3 (3.5 eq.), 120 °C, 3 d; iii) MesMgBr (in tetrahydrofuran, 2.0 eq.), toluene, 0 °C to room temperature.

also work as weak electron donors to the central molecular systems. The lateral expansion of polycyclic DBA scaffold by acenaphthylene (anDBA) or phenanthrene (phenDBA) (Scheme 1) substructures tunes the singlet and triplet excited state energies, enabling extraordinary afterglow properties. This synthetic approach allows for the creation of a colour-tuneable (red and blue to green), ultralong (lifetimes up to 0.8 s and 3.2 s, afterglow duration up to 5 s and 25 s) and efficient (afterglow quantum efficiencies up to 3 % and 15 %) bicomponent organic RT afterglow systems by simply embedding compounds into a rigid poly(methyl methacrylate) (PMMA) matrix. Despite the present RTP of these compounds, the afterglow quantum yield is enhanced by an additional thermally activated delayed fluorescence (TADF) component, which is beneficial in terms of applicability since TADF and RTP exhibit the same long lifetime.[24,25] The pronounced TADF impact to afterglow spectra (especially in the case of phenDBA) also allows to tune the afterglow colour by simply changing the temperature. Even though the explicitly long phosphorescence lifetimes of coronene-h_{12} and coronene-d_{12} based systems in PMMA have already been shown by J. L. Kropp et al.,[26] the presented results in the current work are among the best of recently reported amorphous chromophore-polymer systems, based on simple physical blending.[20,24,25,27–30] The ultralong emission properties of these DBA compounds were further employed for a data-writing demonstration.

Results and Discussion

In order to access anDBA, it was necessary to synthesize 8,9-bis(trimethylsilyl)fluoranthene. This goal could be achieved by applying the Vollhardt-cyclization to 1,8-diethynyl naphthalene. Until now, this known compound could only be prepared under harsh Sonogashira conditions[31] or via HBr elimination from 1,8-bis(1,2-dibromoethyl)naphthalene.[32] In the course of our synthetic efforts, it was found that this versatile building block is accessible via Negishi-coupling of $Me_3SiC{\equiv}CZnCl{\cdot}LiCl$ with 1,8-diiodonaphthalene[33] within 2 h at room temperature in virtually quantitative yield. After desilylation, cyclization and Si/B-exchange, anDBA was obtained in 23 % yield over five steps. The synthesis of phenDBA has already been published elsewhere.[34]

The UV/Vis spectra of anDBA and phenDBA (Figure 1 and Table S1 in Supporting Information) in *c*-hexane are comprised of absorption bands at ca. 330 nm with relatively high molar extinction coefficient values of $\varepsilon \approx 100\,000\ M^{-1}cm^{-1}$ for both compounds and structured bands at ca. 400–455 nm of lower intensity ($\varepsilon \approx 40\,000\ M^{-1}cm^{-1}$). The fluorescence spectra of both compounds also possess vibrationally resolved shapes. For anDBA, the 0 and 1st fluorescence vibronic bands located at 445 nm and 488 nm have a reduced intensity, leaving the 2nd at 520 nm to be the most intense (Figure S4, Supporting Information). According to the evaluated energy difference between bands of anDBA emission spectrum, the peak at 445 nm (2.78 eV) corresponds to a different emitting state than the rest of the observed fluorescence spectrum; however, its contribution to overall emission remains low. In

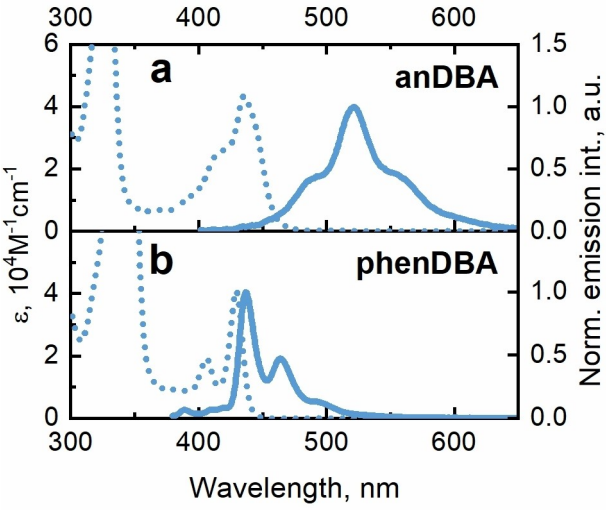

Figure 1. The absorption and fluorescence spectra of anDBA (a) and phenDBA (b) in *c*-hexane at ambient conditions. The concentration of the compounds for fluorescence measurements is 10^{-6} M, the excitation wavelength was set to 330 nm.

the case of phenDBA, a small Stokes shift and mirror image relationship between absorption and fluorescence spectra is observed. The fluorescence quantum yield (Φ_{FL}) of anDBA ($\Phi_{FL}=20\,\%$) is half as high as that of phenDBA ($\Phi_{FL}=47\,\%$), whereas the fluorescence lifetimes (τ) differ three-fold: 14 ns for anDBA and 5 ns for phenDBA (recorded at peak maximum in air saturated, *c*-hexane, see Table S1 in Supporting Information). The performed absorption and fluorescence spectra measurements in solvents of different polarity show no pronounced solvatochromism, revealing the dominant local excitonic (LE) transition for both compounds (Figure S5, Supporting Information). In addition, the degassing of the solutions resulted in a small increase of photoluminescence intensity (ca. 1.3 folds) (Table S1, Supporting Information), caused by the appearance of the weak delayed fluorescence, emphasizing that phosphorescence in solutions is quenched mainly by vibrational relaxation rather than by the oxygen.

The photophysical properties of anDBA and phenDBA compounds in organic solvents appear to be similar to those observed for other laterally expanded dibora-anthracenes.[34,35] However, the studied DBA compounds incorporated in a rigid polymer (PMMA) matrix disclosed the bicomponent delayed emission from the long-lived excited states. The excited state dynamics in a nanosecond to second timescale was revealed by time-resolved emission experiments. The emission decay profiles of 0.1 wt % PMMA encapsulated films and characteristic emission spectra at different time delays are shown in Figure 2a–d. At an early time scale from 0 to 100 ns the prompt fluorescence, peaking at 525 nm for anDBA and at 445–470 nm for phenDBA, is present, with fluorescence lifetimes ($\tau_{FL}=12.5$ ns for anDBA and $\tau_{FL}=8.5$ ns for phenDBA) similar to those observed in solutions. Excitingly, from 1 μs to several seconds, the delayed emission is observed with remarkably long mono-exponential ($\tau_A=0.42$ s) and bi-exponential ($\tau_{A1}=0.17$ s and $\tau_{A2}=0.93$ s) decays for anDBA and phenDBA, respectively, which is referred to as emission afterglow.

The afterglow emission spectra of both compounds are comprised of two bands each: a higher-energy band (at 525 nm for anDBA and 445–470 nm for phenDBA), which is nearly identical to prompt fluorescence spectrum, and a lower-energy band (at 614 nm for anDBA and 531 nm for phenDBA). The origin of the dual afterglow emission is revealed by time-resolved experiments at 30 K (Figure 2c, 2d and Figure S6, Supporting Information). After a significant time delay of 100 μs, the measured low-temperature delayed emission consists of the low-energy part, which is attributed to phosphorescence of compounds. Since the high-energy band, or in other words delayed fluorescence, is temperature dependent and is severely decreased at 30 K, it could originate via thermally activated delayed fluorescence (TADF) or due to triplet-triplet annihilation (TTA). In the case of TTA, the delayed fluorescence at low triplet exciton concentrations should exhibit a lifetime that is twice as short compared to phosphorescence.[36,37] However, the observed dual afterglow emission of DBA compounds has the same ultralong emission lifetimes (Figure S7, Supporting Information), which consequently eliminates TTA, leaving TADF as the most probable origin of delayed fluorescence.

The afterglow quantum yields (Φ_A) at RT obtained by peak-differentiation-imitating analysis for 0.1 wt % PMMA films are 3 % for the red afterglow of anDBA and 15 % for the blue to green afterglow of phenDBA (Table 1). The afterglow quantum yield is a sum of persistent TADF and RTP components ($\Phi_A=\Phi_{TADF}+\Phi_p$). According to the afterglow spectral composition, persistent TADF only slightly contributes to overall afterglow efficiency in the case of anDBA ($\Phi_{TADF}=0.4\,\%$), while in terms of phenDBA, it significantly promotes Φ_A ($\Phi_{TADF}=12\,\%$). The ultralong lifetimes of persistent TADF indicate a very slow reverse intersystem crossing (RISC), that is confirmed by estimated low RISC rate constants: $k_{RISC}=0.05\,s^{-1}$ for anDBA and $k_{RISC}=1.06\,s^{-1}$ for phenDBA.[38] On the other hand, the estimated ISC rates are considerably high: $k_{ISC}=6.0\times10^7\,s^{-1}$ for anDBA and $k_{ISC}=8.4\times10^7\,s^{-1}$ for phenDBA (see Evaluation of rate constants, Supporting Information). The ISC rates match well the non-radiative fluorescence rates obtained in solvents (Table S1, Supporting Information) and indicate the efficient ISC from the excited singlet to excited

Table 1: Emission quantum yields and lifetimes of anDBA and phenDBA, encapsulated in PMMA matrix at different concentrations, measured at room temperature.

wt % in PMMA	anDBA			phenDBA			
	Φ_{PL},[a] %	Φ_A,[b] %	τ_A,[c] s	Φ_{PL},[a] %	Φ_A,[b] %	τ_{A1},[d] s (%)	τ_{A2},[d] s (%)
0.1*[e]	28	3.1	0.42	44	15.1	0.17 (20)	0.93 (80)
1*[e]	20	2.8	0.42	49	11.7	0.39 (24)	1.19 (76)
0.1	30	3.2	0.59	47	11.8	0.21 (17)	1.33 (83)
1	21	2.6	0.70	50	10.3	0.47 (17)	2.60 (83)
5	10	2.3	0.74	47	10.8	0.98 (37)	2.72 (63)
10	11	2.9[f]	0.76	36	7.9[f]	1.00 (25)	3.19 (75)
20	8	1.9[f]	0.71	36	7.3[f]	0.83 (24)	3.06 (76)
40	5	–[g]	–[g]	29	9.2[f]	0.74 (23)	2.97 (77)

[a] Photoluminescence quantum yield including fluorescence and afterglow. [b] Afterglow quantum yield. [c] Afterglow lifetime. [d] Afterglow lifetime components of bi-exponential fit. Fractional contribution of each component is indicated in the parenthesis. [e] Samples that were not annealed prior to experiments. [f] Afterglow quantum yield errors of higher concentration samples may be increased due to aggregation determined processes. [g] The intensity of emission afterglow was too low to accurately record its efficiency and lifetime.

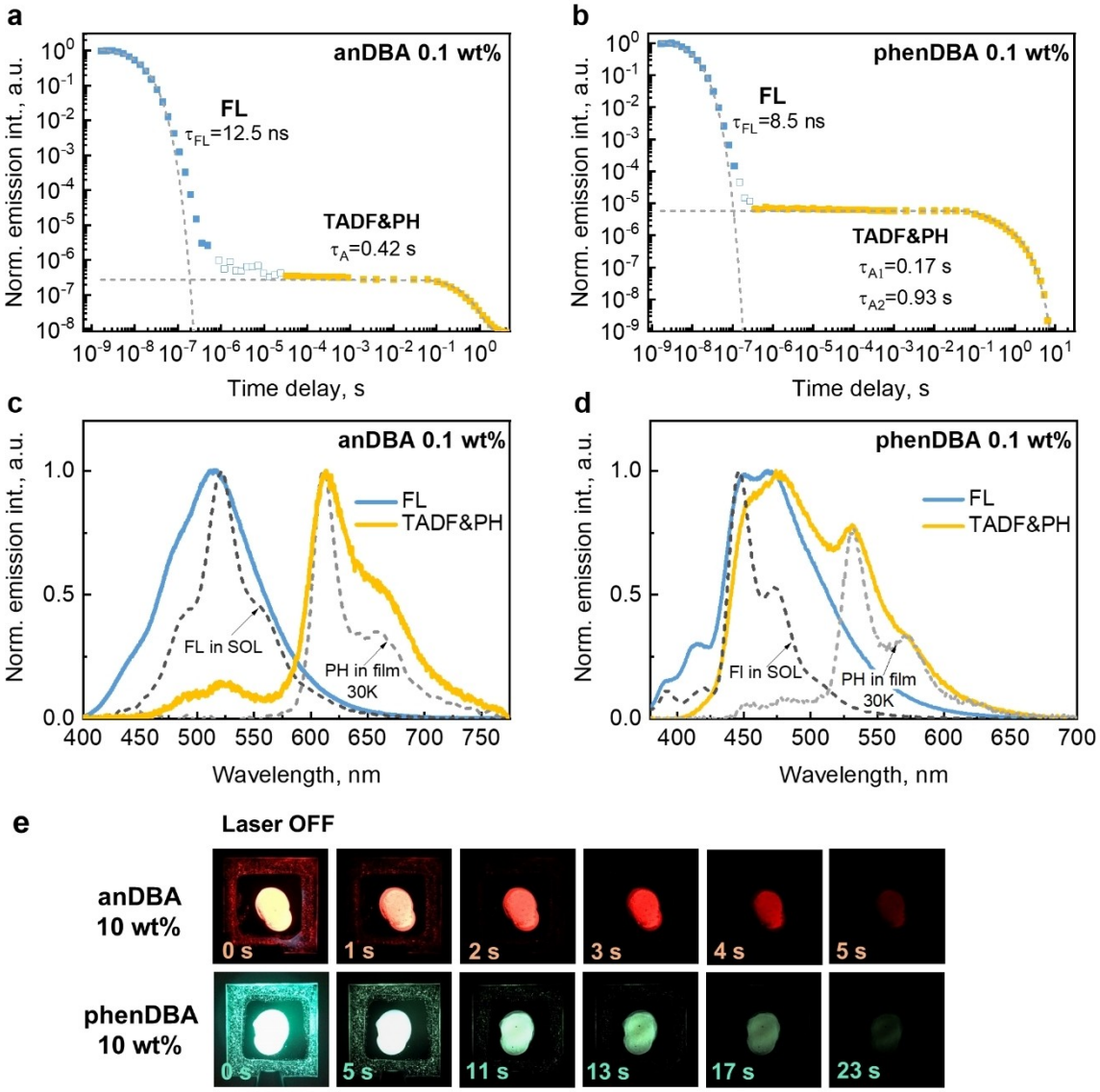

Figure 2. Emission decay transients (a, b) and its characteristic emission spectra (c, d) obtained at different time delays (the FL spectra, blue, at 0–100 ns and TADF&PH spectra, yellow, at 100 μs to few seconds) of anDBA and phenDBA, respectively, in 0.1 wt% encapsulated PMMA films. The excitation wavelength was set to 330 nm. The steady-state fluorescence spectra in *c*-hexane (FL in SOL) and phosphorescence spectra, measured with 100 μs delay and 800 μs optical window of 0.1 wt% PMMA films at 30 K (PH in film 30 K) are also displayed in (c, d) for reference. The photographs of anDBA and phenDBA in 10 wt% encapsulated PMMA films after excitation is turned off (e).

triplet states, which is one of the most important prerequisites for long and efficient afterglow emission.

Thus, despite conflicting in principle, the desired properties of a long and efficient afterglow were demonstrated. Importantly, τ_A can be prolonged even further by annealing the low-concentration PMMA films, since the heat treatment increases rigidity of the PMMA matrix (Table 1). However, the obvious signs of aggregation of the compounds were noted, as PMMA films become opaque once heat-treated. Consequently, we further performed concentration optimization experiments in order to discover the impact of aggregation and the limits of afterglow properties.

Upon increasing the concentration of samples from 0.1 wt% to 40 wt% in PMMA, the small red shift of fluorescence spectra and the redistribution of vibronic band intensity is observed (Figure S8, Supporting Information). The afterglow lifetimes are enhanced up to a certain concentration (10 wt%) and later start to shorten (Table 1, Figure S9, Supporting Information). Most likely, the intermediate to high concentration alters local environment rigidity (compounds act as hardening agents); however, further concentration increase enhances exciton diffusion to non-radiative deactivation sites such as impurities or structural defects. The longest emission afterglow, observed for 10 wt% PMMA samples, reaches up to $\tau_A = 0.76$ s and up to $\tau_{A1} = 1$ s, $\tau_{A2} = 3.19$ s, with considerably long afterglow durations (time until the afterglow is no longer visible to the naked eye) of 5 s and 25 s for anDBA and phenDBA,

respectively (Table 1, Figure 2e and Movie S1). It has already been shown elsewhere that the morphology of samples may be critical to obtain long and efficient RTP (or afterglow).[39] However, it is debatable whether the emission afterglow in the current work is related to H-aggregation (or π-π stacking) as a typical mechanism of ultralong RTP.[12–16] Even though the increase of afterglow lifetimes was observed in films containing a higher concentration of the dopant, the absence of phosphorescence spectral shift in 10 wt % PMMA films, compared to 0.1 wt % (Figure S10, Supporting Information), rules out the possible stabilization of triplet states upon molecular aggregation. It is important to note that the slow evaporation of solvent due to selected preparation method (drop-casting) may cause the aggregation of chromophores, especially considering the large π-conjugated structures of studied compounds. Thus, the control measurements were repeated on the spin-coated thin film samples of 0.1 wt % in PMMA (see Figure S11, Supporting Information) in order to presumably avoid aggregation and to check the appearance of afterglow emission. Indeed, the obtained afterglow lifetimes (τ_A = 0.45 s for anDBA and τ_{A1} = 0.16 s, τ_{A2} = 1.35 s for phenDBA) are similar to those of drop-casted 0.1 wt % PMMA films. These results suggest that the ultralong afterglow arises due to properties of single molecules, in contrast to, for example, charge-separation based afterglow systems, where exciplexes need to be formed between a host and guest molecules in order to realize long afterglow durations, that may last up to hours.[40]

To comprehend the role of the excited state energy levels arrangement and other structure-related properties on bi-component emission afterglow of studied DBA compounds, the theoretical evaluation was further performed. The ground state and the selected excited state (S_1, S_2, S_3 and T_1) geometries as well as transition energies were calculated by using Tamm-Dancoff approximation (TDA)[41] to TD-DFT at the theory level of CAMB3LYP/6-31G(d), implemented in ORCA 5.0.3 software,[42,43] including linear response polarized continuum model (LR-PCM, solvent-toluene). Although the range-separated functionals tend to overestimate LE state energies, it was employed as a qualitative tool to evaluate the energetical arrangement and thus the energetical difference between states, as well as molecular orbital redistribution, especially as the upper triplet (as well as singlet) states appear to be of charge transfer (CT) nature (see below).[35,44] According to the obtained charge distribution in HONTO and LUNTO states (Figure 3 and Figures S13–S14, Supporting Information), acenaphthylene units determine more extended conjugation in the polycyclic scaffold of anDBA if compared to phenDBA, which is laterally expanded by phenanthrene units decorated with *tert*-butyl groups. The extended conjugation itself determines the lower energies of excited states of anDBA and thus, the red shifted fluorescence and phosphorescence spectra. The differences in conjugation

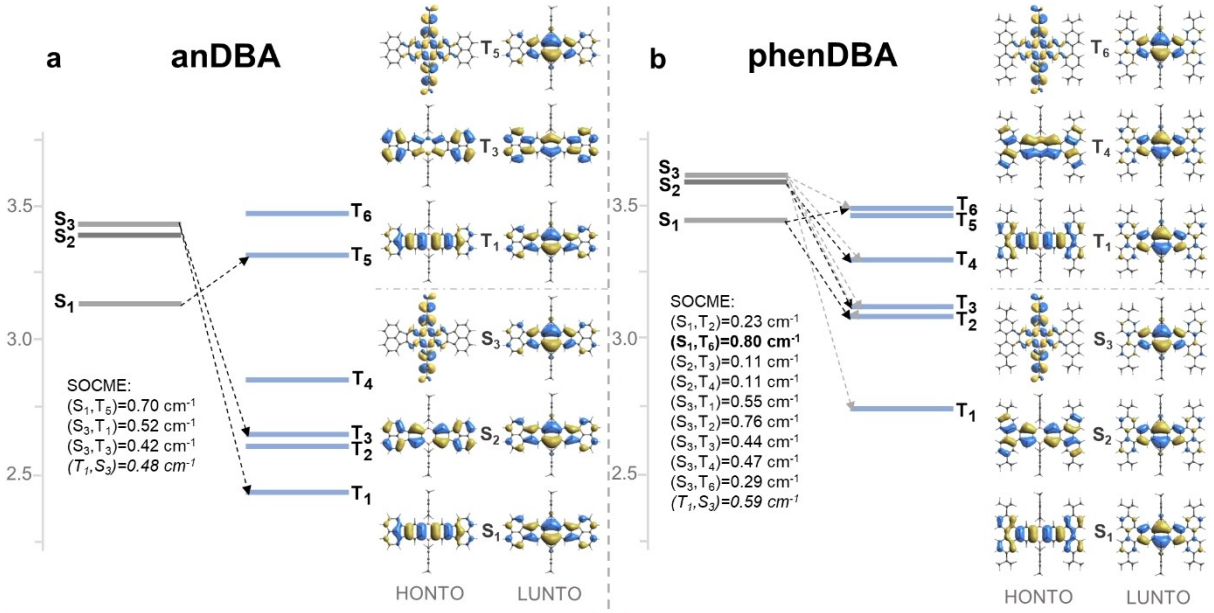

	S_1	S_2	S_3
E, eV (*f*)	3.14 (*0*)	3.40 (*1.36*)	3.43 (*0*)

T_1	T_2	T_3	T_4	T_5	T_6
2.44	2.61	2.65	2.85	3.32	3.47

	S_1	S_2	S_3
E, eV	3.45 (*0*)	3.59 (*0.80*)	3.61 (*0*)

T_1	T_2	T_3	T_4	T_5	T_6
2.74	3.09	3.12	3.30	3.46	3.49

Figure 3. The singlet-triplet energy diagram, the corresponding $S_0 \rightarrow S_n$ and $S_0 \rightarrow T_n$ energies in eV, oscillator strengths of $S_0 \rightarrow S_n$ transitions and natural transition orbital (NTO) distribution, obtained for optimized ground state geometries, for anDBA (a) and phenDBA (b). The arrows indicate spin-orbit coupling between states, which was obtained for optimized S_1, S_2 and S_3 and T_1 excited state geometries.

length may be defined by electron donoric properties of *tert*-butyl groups, causing a more localized charge distribution on the dibora core in LUNTO states of phenDBA.

The performed calculations revealed a multitude of nearby lying singlet and triplet states (Figure 3, Tables S2 and S4, Supporting Information). The calculated lowest excited singlet states S_1 in a ground state geometry were found to be forbidden "dark" states with oscillator strength (f) equal to zero for both compounds, mainly due to the lack of corresponding HONTO-LUNTO wavefunction overlap (see molecular orbital distribution in Figure 3 and in Figures S13–S14, Supporting Information), as was also observed elsewhere for a similar 6,13-dimesityl-6,13-dihydro-6,13-diborapentacene compound.[35] The first "bright" states, also observed as the lowest energy absorption bands in the absorption spectra, with significant oscillator strengths of $f=1.36$ for anDBA and $f=0.80$ for phenDBA are S_2 states, where charge is mainly located on the polycyclic core in the ground state and is redistributed to the dibora core upon excitation. Both S_1 and S_2 possess a LE character. Interestingly, almost degenerate states for locally excited S_2 are the S_3 states of charge transfer nature, where charge from mesityl groups is transferred to the dibora core. The optimization of the excited S_1, S_2 and S_3 geometries revealed that the lowest excited states, after molecular geometry relaxation, remain the forbidden S_1 states. However, in the case of phenDBA, the oscillator strength for S_1-S_0 transition acquires a non-zero oscillator strength value of 0.004. According to Figure 3, there are at least six excited triplet states that lie energetically close or below S_1-S_3 singlet states. The lowest triplet states T_1 are comprised of the same charge distribution in the HONTO and LUNTO states as S_1. Most of the triplet states that lay higher than T_1 also possess LE nature. However, the T_5 and T_6 for anDBA and phenDBA, respectively, are both of CT nature, with similar charge redistribution as for S_3 states.

The efficient emission afterglow and relatively short fluorescence lifetimes discussed in the previous section suggest an efficient intersystem crossing (ISC). The spin-orbit coupling (SOC) between singlet and triplet states were calculated for the optimized S_1, S_2, S_3 and T_1 excited state geometries for the respective $S_n \rightarrow T_n$ and $T_1 \rightarrow S_n$ transitions and are indicated for reference in Figure 3 and given in Tables S3 and S5, Supporting Information. In the case of anDBA, the highest SOC matrix element value (SOCME) was obtained for $S_1 \rightarrow T_5$ transition (SOCME = 0.70 cm^{-1}). Alternatively, significant SOCMEs were also obtained for $S_3 \rightarrow T_1$ (0.52 cm^{-1}) or $S_3 \rightarrow T_3$ (0.42 cm^{-1}) transitions, though the energy gap difference would be higher in the latter case. Nevertheless, it is obvious that CT states, whether singlet or triplet, play a crucial role in terms of ISC for anDBA. In the case of phenDBA, the possible multichannel ISC is estimated. The highest spin-orbit coupling is calculated for $S_1 \rightarrow T_6$ transition with SOCME = 0.80 cm^{-1}. In addition, the CT S_3 state efficiently couples with almost all triplet states. No spin-orbit coupling between S_1 and T_1 is obtained for either compound, as expected due to the same electronic character. The spin-orbit coupling was only considered for excited states up to S_3, as no significant changes of the excited state dynamics were observed by exciting anDBA or phenDBA samples at 330 nm or at 440 nm.

The immensely long lifetimes of the lowest excited triplet states, the existence of multiple intermediate triplet states and the relatively large SOCME values between S_n and T_n states also explain the presence of TADF, even though the significantly large $\Delta E(S_1\text{-}T_1)$ gaps (> 500 meV (anDBA) and 440 meV (phenDBA)) are revealed experimentally from fluorescence and phosphorescence spectra and confirmed theoretically (Figure S6 and Tables S2 and S4, Supporting Information). According to the Arrhenius plots obtained from TADF spectral integral dependence on the reciprocal temperature, the activation energy (E_a) is equal to 160 meV for anDBA, while for phenDBA two E_a values were obtained: 115 meV at low temperatures and 57 meV at higher temperatures (Figure 4a–d). We suggest that the mismatch between $\Delta E(S_1\text{-}T_1)$ and E_a most likely indicates that TADF is enabled through intermediate triplet states, as it is quite frequently observed for other TADF-type emitters.[45–48] Furthermore, in case the activation

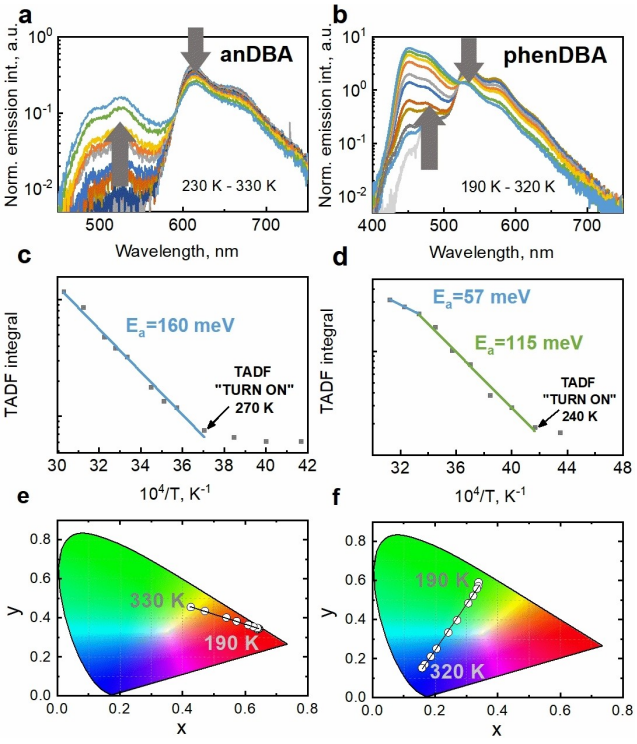

Figure 4. The afterglow spectra of anDBA (a) and phenDBA (b) in 1 wt% PMMA, measured after 100 μs delay and with 800 μs optical window, at different temperatures. The grey arrows in a and b represent the increase or decrease of afterglow intensity upon temperature increase (230–330 K for anDBA and 190–320 K for phenDBA). The respective Arrhenius plots, obtained by plotting TADF spectral integral versus reciprocal temperature, with activation energies, obtained from linear fits (blue and green lines), given in graphs for anDBA (c) and phenDBA (d). Samples of 1 wt% in PMMA were selected in order to facilitate measurement conditions by obtaining higher intensity of afterglow and also to avoid aggregation induced effects. The CIE chromaticity diagrams representing the dependence of afterglow colour on different temperatures for anDBA (e) and phenDBA (f).

energy reflects the adiabatic $\Delta E(S_1\text{-}T_1)$, the RISC between S_1 and T_1 would be highly restricted due to the same electronic nature of S_1 and T_1 and thus the absent SOC between these two states. The unusual dual activation energy of phenDBA may indicate different RISC channels.

The presence of persistent TADF component in the afterglow spectra and its intensity dependence on temperature results in the possibility to tune afterglow colour for studied compounds. The CIE (x, y) chromaticity coordinates change significantly: from (0.64, 0.34) at 190 K to (0.43, 0.45) at 330 K for anDBA and from (0.34, 0.59) at 190 K to (0.16, 0.15) at 320 K for phenDBA (see Figure 4e and 4f).

The estimated radiative phosphorescence rates $k_p = 0.06\ s^{-1}$ and $k_p = 0.04\ s^{-1}$ ($k_p = \Phi_p/\tau_A$) for anDBA and phenDBA, respectively, in 0.1 wt % PMMA at RT are sufficiently low. However, to observe the ultralong phosphorescence, the negligible non-radiative phosphorescence rates (k_{nr}) are also needed.[1] Indeed, the long-lived T_1 states are defined by the very low k_{nr} values: $k_{nr} = 2.3\ s^{-1}$ for anDBA and $k_{nr} = 1.2\ s^{-1}$ for phenDBA ($k_{nr} = [1\text{-}\Phi_p]/\tau_A$). This may be related to the weak electron-vibronic interaction caused by the localization of the excited states on the dibora core (in the excited T_1 geometry). Interestingly, the phosphorescence rates are significantly reduced (lifetimes prolonged) below TADF "turn-on" temperatures (270 K for anDBA and 240 K for phenDBA) (Figure S12, ESI), indicating that TADF actually acts as the main depopulation channel of the lowest excited triplet states at RT, while simultaneously increasing the afterglow quantum efficiency. The roughly estimated non-radiative phosphorescence rates at low temperatures (230 K, for 1 wt % PMMA films) are extremely small: $k_{nr} \approx 1\ s^{-1}$ for anDBA and $k_{nr} \approx 0.2\ s^{-1}$ for phenDBA. Thus, the rigidity of polymer matrix is sufficient to practically reach the limits of phosphorescence k_{nr}, which is also related to molecular properties, such as low vibronic coupling between the lowest excited triplet and ground states.[49]

Thus, we believe that the nature of such extraordinary triplet non-radiative decay rates deserves a separate study in order to better understand the design principles of single molecules for ultralong and efficient room temperature phosphorescence. In addition, the wide possibilities to adjust DBA structure by changing electron donating fragments or by incorporating different lateral substituents should help to fine-tune the energetical alignment for the desired properties, i.e. turning off TADF for even longer phosphorescence or, contrarily, enhancing long-lived delayed fluorescence for higher afterglow efficiencies.

The properties of the studied compounds were further tested for information recording. First, the transparent films were prepared by coating thin DBA layers of 0.2 wt % in PMMA on a glass and covering them with poly(vinyl alcohol) (PVA) layers that serve as an oxygen barrier. As the procedure is carried out in ambient conditions, only fluorescence is present upon excitation of films. Next, the samples were irradiated by 405 nm laser light (>5 mW power) through a selected mask for a certain time (≈1 min), until the intense phosphorescence was observed in an oxygen saturated environment. The selected information writing method is based on the control of molecular oxygen in chromophore-polymer film, as presented elsewhere.[50] Once excited, DBA compounds generate high triplet exciton concentration, which is quenched by molecular oxygen trapped in a polymer. Upon quenching, the singlet oxygen is generated, which mostly reacts with surrounding polymer and thus the depleted oxygen concentration leads to efficient phosphorescence in the irradiated area. The written information can be further read by changing the irradiation intensity to a low level (alternatively, a CW light source can be used), as only regions that were previously strongly irradiated are glowing. Consequently, two tags of different colours with encrypted information were prepared with visible red and cyan afterglow emission up to 2 s and 8 s, for anDBA and phenDBA, respectively (Figure 5 and Movie S2).

Conclusion

In summary, we have presented two laterally expanded 9,10-dimesityl-9,10-diboraanthracenes (DBA) by acenaphthylene and phenanthrene units with weak electron donating mesityl groups as a new class of purely organic room temperature afterglow materials. The ultralong and efficient emission afterglow is comprised of persistent TADF and RTP, with lifetimes of up to 0.8 s and 3.2 s, afterglow duration up to 5 s and 25 s, and maximum afterglow quantum efficiencies up to 3 % and 15 % for red and blue to green emitters, respectively. The afterglow emission originates from single molecules embedded into rigid polymer (PMMA) matrix, rather than from aggregated molecular states. On the other hand, the emission properties can be tuned upon annealing or increasing the compound concentration. The afterglow mechanism is a combination of i) the multiple available channels for an efficient ISC between excited singlet and triplet states of different nature; ii) the lowest excited LE triplet states (T_1) with very low radiative and non-radiative decay rates; and finally, iii) closely lying triplet and singlet states as well as long-lived population of T_1 that both create the possibility for reverse intersystem crossing, causing the appearance of TADF component through intermediate states. TADF is considered to be the main depopulation channel of the lowest excited triplet states at room temper-

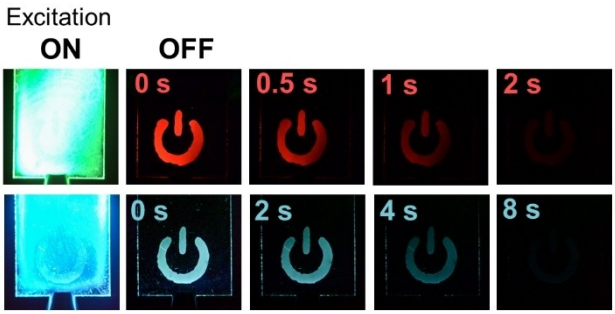

Figure 5. The afterglow images of recorded data on anDBA (top) and phenDBA (bottom) 0.2 wt % PMMA transparent layers.

ature, while it significantly increases the afterglow efficiency. Besides, the presence of persistent TADF allows tuning the afterglow colour, which may be advantageous for temperature sensing. The ultralong-lived emission properties of studied molecules were successfully employed for data writing. The presented DBA compounds demonstrate the superior afterglow properties, especially compared to other amorphous chromophore-polymer systems. Our strategy allows for a wide range of synthetic possibilities to fine-tune the RT afterglow by incorporating stronger electron donors and/or by introducing different lateral substituents.

Acknowledgements

We wish to thank Klara R. Mertinkus, BSc., for synthetic support, Dr. Tomas Serevičius for the insightful discussions at the early stages of this project and Dr. Rokas Skaisgiris for the technical upgrade of equipment for spectroscopic measurements. We also thank Dr. Jan-Michael Mewes for the helpful discussion regarding theoretical calculations. The research was funded by the European Social Fund (Project No. 09.3.3-LMT-K-712-23-0053) under a grant agreement with the Research Council of Lithuania (LMTLT). Open Access funding enabled and organized by Projekt DEAL.

Conflict of Interest

The authors declare no conflict of interest.

Data Availability Statement

The data that support the findings of this study are available from the corresponding author upon reasonable request.

Keywords: Afterglow · Doped Polymer Films · Information Recording · Room Temperature Phosphorescence · Thermally Activated Delayed Fluorescence

[1] S. Xu, R. Chen, C. Zheng, W. Huang, S. Xu, R. Chen, C. Zheng, W. Huang, *Adv. Mater.* **2016**, *28*, 9920–9940.
[2] Y. Su, S. Z. F. Phua, Y. Li, X. Zhou, D. Jana, G. Liu, W. Q. Lim, W. K. Ong, C. Yang, Y. Zhao, *Sci. Adv.* **2018**, *4*, eaas9732.
[3] L. Gu, H. Wu, H. Ma, W. Ye, W. Jia, H. Wang, H. Chen, N. Zhang, D. Wang, C. Qian, Z. An, W. Huang, Y. Zhao, *Nat. Commun.* **2020**, *11*, 944.
[4] Y. Lei, W. Dai, J. Guan, S. Guo, F. Ren, Y. Zhou, J. Shi, B. Tong, Z. Cai, J. Zheng, Y. Dong, *Angew. Chem. Int. Ed.* **2020**, *59*, 16054–16060; *Angew. Chem.* **2020**, *132*, 16188–16194.
[5] F. Xiao, H. Gao, Y. Lei, W. Dai, M. Liu, X. Zheng, Z. Cai, X. Huang, H. Wu, D. Ding, *Nat. Commun.* **2022**, *13*, 186.
[6] X. Li, C. Yin, S. S. Liew, C.-S. Lee, K. Pu, X. Li, C.-S. Lee, C. Yin, S. S. Liew, K. Pu, *Adv. Funct. Mater.* **2021**, *31*, 2106154.
[7] S. Hirata, *Adv. Opt. Mater.* **2017**, *5*, 1700116.
[8] H. Ma, Q. Peng, Z. An, W. Huang, Z. Shuai, *J. Am. Chem. Soc.* **2019**, *141*, 1010–1015.
[9] M. A. El-Sayed, *J. Chem. Phys.* **1963**, *38*, 2834–2838.
[10] J. T. Buck, A. M. Boudreau, A. DeCarmine, R. W. Wilson, J. Hampsey, T. Mani, *Chem* **2019**, *5*, 138–155.
[11] C. M. Marian, *Wiley Interdiscip. Rev.: Comput. Mol. Sci.* **2012**, *2*, 187–203.
[12] W. Zhao, Z. He, B. Z. Tang, *Nat. Rev. Mater.* **2020**, *5*, 869–885.
[13] L. Gu, H. Shi, L. Bian, M. Gu, K. Ling, X. Wang, H. Ma, S. Cai, W. Ning, L. Fu, H. Wang, S. Wang, Y. Gao, W. Yao, F. Huo, Y. Tao, Z. An, X. Liu, W. Huang, *Nat. Photonics* **2019**, *13*, 406–411.
[14] W. Jia, Q. Wang, H. Shi, Z. An, W. Huang, *Chem. Eur. J.* **2020**, *26*, 4437–4448.
[15] Z. An, C. Zheng, Y. Tao, R. Chen, H. Shi, T. Chen, Z. Wang, H. Li, R. Deng, X. Liu, W. Huang, *Nat. Mater.* **2015**, *14*, 685–690.
[16] A. Forni, E. Lucenti, C. Botta, E. Cariati, *J. Mater. Chem. C* **2018**, *6*, 4603–4626.
[17] S. Guo, W. Dai, X. Chen, Y. Lei, J. Shi, B. Tong, Z. Cai, Y. Dong, *ACS Mater. Lett.* **2021**, *3*, 379–397.
[18] X. K. Ma, Y. Liu, *Acc. Chem. Res.* **2021**, *54*, 3403–3414.
[19] Y. Gong, J. Yang, M. Fang, Z. Li, *Cell Rep. Phys. Sci.* **2022**, *3*, 100663.
[20] Y. Zhang, Y. Su, H. Wu, Z. Wang, C. Wang, Y. Zheng, X. Zheng, L. Gao, Q. Zhou, Y. Yang, X. Chen, C. Yang, Y. Zhao, *J. Am. Chem. Soc.* **2021**, *143*, 13675–13685.
[21] J. Guo, C. Yang, Y. Zhao, *Acc. Chem. Res.* **2022**, *55*, 1160–1170.
[22] C. Hoffend, M. Diefenbach, E. Januszewski, M. Bolte, H. W. Lerner, M. C. Holthausen, M. Wagner, *Dalton Trans.* **2013**, *42*, 13826–13837.
[23] C. Reus, S. Weidlich, M. Bolte, H. W. Lerner, M. Wagner, *J. Am. Chem. Soc.* **2013**, *135*, 12892–12907.
[24] X. Wang, Y. Sun, G. Wang, J. Li, X. Li, K. Zhang, *Angew. Chem. Int. Ed.* **2021**, *60*, 17138–17147; *Angew. Chem.* **2021**, *133*, 17275–17284.
[25] M. Louis, H. Thomas, M. Gmelch, A. Haft, F. Fries, S. Reineke, *Adv. Mater.* **2019**, *31*, 1807887.
[26] J. L. Kropp, W. R. Dawson, *J. Phys. Chem.* **1967**, *71*, 4499–4506.
[27] Z. Ma, Z. Yang, L. Mu, L. Deng, L. Chen, B. Wang, X. Qiao, D. Hu, B. Yang, D. Ma, J. Peng, Y. Ma, *Chem. Sci.* **2021**, *12*, 14808–14814.
[28] M. Jian, Z. Song, X. Chen, J. Zhao, B. Xu, Z. Chi, *Chem. Eng. J.* **2022**, *429*, 132346.
[29] Y. Yang, Y. Liang, Y. Zheng, J. A. Li, S. Wu, H. Zhang, T. Huang, S. Luo, C. Liu, G. Shi, F. Sun, Z. Chi, B. Xu, *Angew. Chem. Int. Ed.* **2022**, *61*, e202201820; *Angew. Chem.* **2022**, *134*, e202201820.
[30] X. Yan, H. Peng, Y. Xiang, J. Wang, L. Yu, Y. Tao, H. Li, W. Huang, R. Chen, X. Yan, H. Peng, Y. Xiang, J. Wang, L. Yu, Y. Tao, H. Li, W. Huang, R. Chen, *Small* **2022**, *18*, 2104073.
[31] X. Liu, Q. Yi, Y. Han, Z. Liang, C. Shen, Z. Zhou, J. Sun, Y. Li, W. Du, R. Cao, *Angew. Chem. Int. Ed.* **2015**, *54*, 1846–1850; *Angew. Chem.* **2015**, *127*, 1866–1870.
[32] R. H. Mitchell, F. Sondheimer, *Tetrahedron* **1968**, *24*, 1397–1405.
[33] M. Weimar, G. Dürner, J. W. Bats, M. W. Göbel, *J. Org. Chem.* **2010**, *75*, 2718–2721.
[34] A. John, S. Kirschner, M. K. Fengel, M. Bolte, H. W. Lerner, M. Wagner, *Dalton Trans.* **2019**, *48*, 1871–1877.
[35] S. Kirschner, J.-M. Mewes, M. Bolte, H.-W. Lerner, A. Dreuw, M. Wagner, *Chem. Eur. J.* **2017**, *23*, 5104–5116.
[36] A. Köhler, H. Bässler, *Mater. Sci. Eng. R* **2009**, *66*, 71–109.
[37] A. Hayer, H. Bässler, B. Falk, S. Schrader, *J. Phys. Chem. A* **2002**, *106*, 11045–11053.
[38] Y. Tsuchiya, S. Diesing, F. Bencheikh, Y. Wada, P. L. dos Santos, H. Kaji, E. Zysman-Colman, I. D. W. Samuel, C. Adachi, *J. Phys. Chem. A* **2021**, *125*, 8074–8089.

[39] S. Reineke, M. A. Baldo, *Sci. Rep.* **2014**, *4*, 3797.
[40] Z. Lin, R. Kabe, N. Nishimura, K. Jinnai, C. Adachi, Z. Lin, R. Kabe, N. Nishimura, K. Jinnai, C. Adachi, *Adv. Mater.* **2018**, *30*, 1803713.
[41] S. Hirata, M. Head-Gordon, *Chem. Phys. Lett.* **1999**, *314*, 291–299.
[42] F. Neese, *Wiley Interdiscip. Rev.: Comput. Mol. Sci.* **2012**, *2*, 73–78.
[43] F. Neese, *Wiley Interdiscip. Rev.: Comput. Mol. Sci.* **2022**, *12*, e1606.
[44] J. Plötner, D. J. Tozer, A. Dreuw, *J. Chem. Theory Comput.* **2010**, *6*, 2315–2324.
[45] F. B. Dias, K. N. Bourdakos, V. Jankus, K. C. Moss, K. T. Kamtekar, V. Bhalla, J. Santos, M. R. Bryce, A. P. Monkman *Adv. Mater.* **2013**, *25*, 3707–3714.
[46] J. Gibson, T. J. Penfold, *Phys. Chem. Chem. Phys.* **2017**, *19*, 8428–8434.
[47] T. Serevičius, R. Skaisgiris, I. Fiodorova, G. Kreiza, D. Banevičius, K. Kazlauskas, S. Tumkevičius, S. Juršėnas, *J. Mater. Chem. C* **2021**, *9*, 836–841.
[48] H. Noda, X. K. Chen, H. Nakanotani, T. Hosokai, M. Miyajima, N. Notsuka, Y. Kashima, J. L. Brédas, C. Adachi, *Nat. Mater.* **2019**, *18*, 1084–1090.
[49] H. Ma, H. Yu, Q. Peng, Z. An, D. Wang, Z. Shuai, *J. Phys. Chem. Lett.* **2019**, *10*, 6948–6954.
[50] M. Gmelch, H. Thomas, F. Fries, S. Reineke, *Sci. Adv.* **2019**, *5*, eaau7310.

Manuscript received: October 13, 2022
Accepted manuscript online: November 22, 2022
Version of record online: December 14, 2022